International Journal of Mechanical Sciences 224 (2022) 107325

Contents lists available at ScienceDirect

International Journal of Mechanical Sciences

journal homepage: www.elsevier.com/locate/ijmecsci

Mass-spring model of elastic media with customizable willis coupling

Hongfei Qu, Xiaoning Liu *, Gengkai Hu

School of Aerospace Engineering, Beijing Institute of Technology, Beijing 100081, P.R. China

ARTICLE INFO

Key words:
Elastic metamaterial
Willis coupling
Material design
Mode conversion

ABSTRACT

Willis coupling, in context of acoustics or elasticity designating the coupling between the strain and momentum, have been garnering significant attentions in recent years. As opposed to various applications demonstrated for acoustic wave, elastic media design with Willis coupling on demand is very rare. In this paper, based on a mass-spring model, the accessibility of various components of the coupling tensor for elastic Willis media is explored, and material design with customized Willis coupling aiming to elastic wave control is demonstrated. Homogenization and designability of the model are at first validated via the free wave analysis, then wave transmission properties across a sandwiched Willis layer are analyzed, based on which two illustrative examples for asymmetric reflection and wave mode conversion are demonstrated by specifically designed lattice model. Though the model is conceptual and still far away from practical usage, it may inspire more practical design and further explorations on realizing wave rectification by Willis materials.

1. Introduction

Metamaterials are artificial composite materials constructed with deliberately designed microstructures and possess extraordinary material properties usually not found in natural ones. In the realm of acoustics or elastodynamics, unconventional properties such as negative bulk modulus [1], negative or anisotropic mass density [2,3] have been demonstrated. Besides, common constraints on the major or minor symmetry of an elastic tensor may also be broken [4,5]. These have enabled unprecedented wave phenomena and applications i.e. negative refraction [6,7], superlensing [8,9], cloaking [4,10,11] and so on.

For metamaterials, the relationship between material parameters and physical fields has exceeded the coverage of the classical acoustic and Cauchy elastic media in many cases, appealing a more comprehensive constitutive relationship. In this background, the theory of Willis materials, initially proposed by Willis [12] in 1980's to characterize the overall elastodynamic behavior of composite materials via ensemble average, has regained the attention and been revisited by many researchers. Willis materials incorporate additional terms in the constitutive relation inducing local coupling of potential and kinetic energy at a material point, in analogy to the so called bianisotropy for electromagnetism. For elasticity, another stimulus for research of Willis media is that it conforms with the elastic cloaking theory derived with the covariant transformation gauge [13,14].

In line with the metamaterials and phononic crystals, recent studies on Willis homogenization are more focused on periodic media and interpret the ensemble average with volume average of Bloch wave amplitude [15–21]. Sieck et al. [22] introduced a homogenization theory for acoustic Willis media based on the point polarization approximation in analogy with that of electromagnetism [23]. The approach also reveals that the imaginary part of acoustic Willis effect is due to the coupling of monopole and dipole moment induced by an asymmetric scatterer, while the real part originates from the finite phase speed as the wave traverse the unit cell [22,23]. It is interesting to note that some other methods for dynamic homogenization are also related to the Willis theory. Craster et al. [24–27] generalized asymptotic homogenization theory to higher frequencies through expansion at the standing wave points of Bloch wave bands. Nassar et al. [28] showed that, under appropriate approximation assumptions, a series of asymptotic homogenization approaches can be derived from Willis homogenization for periodic media. Sridhar et al. [29–31] developed the micromorphic homogenization for metamaterials, in which projection functions formulated by Bloch eigenvectors are used to capture the high frequency dynamics. The same coupling terms also appear in that approach.

Since the point polarization approximation theory was developed, a number of acoustic meta-atoms exhibiting Willis coupling have been proposed based on different mechanisms, such as the membrane unit [32,33], folded channel [34], Helmholtz resonators [35,36]. Besides, active mechanisms can also be introduced in to enhance the significance and flexibility of the coupling effect [37,38]. Due to the extra degree of

* Corresponding author at: Xiaoning Liu, Beijing Institute of Technology. No. 5, Zhongguancun South Street, Haidian District, Beijing, 100081, P.R. China.
E-mail address: liuxn@bit.edu.cn (X. Liu).

https://doi.org/10.1016/j.ijmecsci.2022.107325
Received 20 March 2022; Received in revised form 1 May 2022; Accepted 2 May 2022
Available online 6 May 2022

freedom of design offered by the Willis coupling, various applications were explored for enhanced wave functionalities. The most widely explored property is the flexible control of transmission and reflection coefficients. Several studies [33,39-41] have observed the asymmetric reflection phases when waves are incident on the Willis media from different directions. If the loss is considered, the reflection amplitude and sound absorption will also exhibit asymmetry [42–44], base on which the unidirectional perfect absorber maybe realized. In nonreciprocal systems, the Willis coupling may also cause asymmetric transmission. Active units are used to realize unidirectional sound isolation [45,46]. In some other studies [47–50], the reciprocity is broken by material nonlinearity and structural asymmetry to exhibit asymmetric transmission, however, how to characterize the nonlinearity related nonreciprocity through the Willis coupling is still to be explored. The tunability of transmission and reflection offered by Willis coupling is of great importance for the wavefront control, which can lead to higher efficiency when used in metasurfaces [32,51-53] or metagratings [34,54,55] for anomalous refraction or reflections. Other wave properties in Willis acoustic media, such as the sound scattering [56], sound focusing [57], the topological phase transition [58], the radiation force and torque [59] have also been investigated.

When it comes to elastic materials, corresponding Willis material design with envisaged functionality is rarely demonstrated. As opposed to acoustics, monopole and dipole scattering are not enough to express the elastic meta-atom in presence of shear, consequently there is not yet a full picture for the Willis coupling, especially when anisotropy is taken into account. So far, the lack of mechanism and the spatio-temporal nonlocality of investigated model makes it difficult to use in a functionality design. Some concrete elastic Willis material design were carried out for bending waves in beams or plates [40,53], while corresponding designs aiming at manipulation of bulk elastic waves are very few. Besides the usual continuum configuration, Milton [60] constructed a theoretical lumped-parameter model consisting of ideal springs, rigid bars and mass points. The model is easy to be understood while at the same time exhibits significant Willis coupling effect together with longwave homogenization. Though the model was not validated in a wave environment, it serves as an ideal platform to customize the complex pattern of properties of an elastic Willis medium. Currently, there is no elastic Willis material design aiming at realizing demanded pattern of the coupling tensor.

In order to provide an Willis material design for targeted elastic wave control, and in particular to explore the accessibility of various components of the elastic Willis coupling tensor, we extend in this paper the model in ref. [60] to cover more components of the effective Willis coupling tensor. Further, we show that by appropriate model combination, desired Willis material properties can be hopefully achieved as required by specific wave functionalities. The homogenization and coupling effect are verified by dispersion analysis and wave transmission across a layer. The paper is organized as follows. In Section 2, the effective properties of the proposed elastic Willis model under different configurations are discussed. Section 3 presents free wave analysis of the model, and specific microstructures are verified. In Section 4, wave transmission through a sandwiched Willis material layer is analyzed in conjunction with two examples of wave manipulation. Finally, conclusions will be drawn in Section 5.

2. The mass-spring model with willis coupling in longwave limit

In this section we will generalize the mass-spring model originally devised by Milton [60], and will fully explore its accessibility to various components of Willis coupling tensor via configuration variation or model combination. Effective material parameters will be explicitly connected to the microstructure parameters with appropriate homogenization.

As shown in Fig. 1, the model is composed of concentrated mass points and massless springs and rigid rods. The model can be thought of as a background spring network with one or several coupling elements attached on it. Square spring network with characteristic scale h is used here although other lattice types can be also adopted. A single coupling element consists of a mass m_E joined by two rigid bars with the ends selectively sitting at two of the four boundary sites A∼D in the unit cell. For a certain location of mass m_E inside the unit cell, we have six choices of bar attachment, i.e. on the AC, AB, AD, BD, CB and CD sites, each results in different effect to the effective properties.

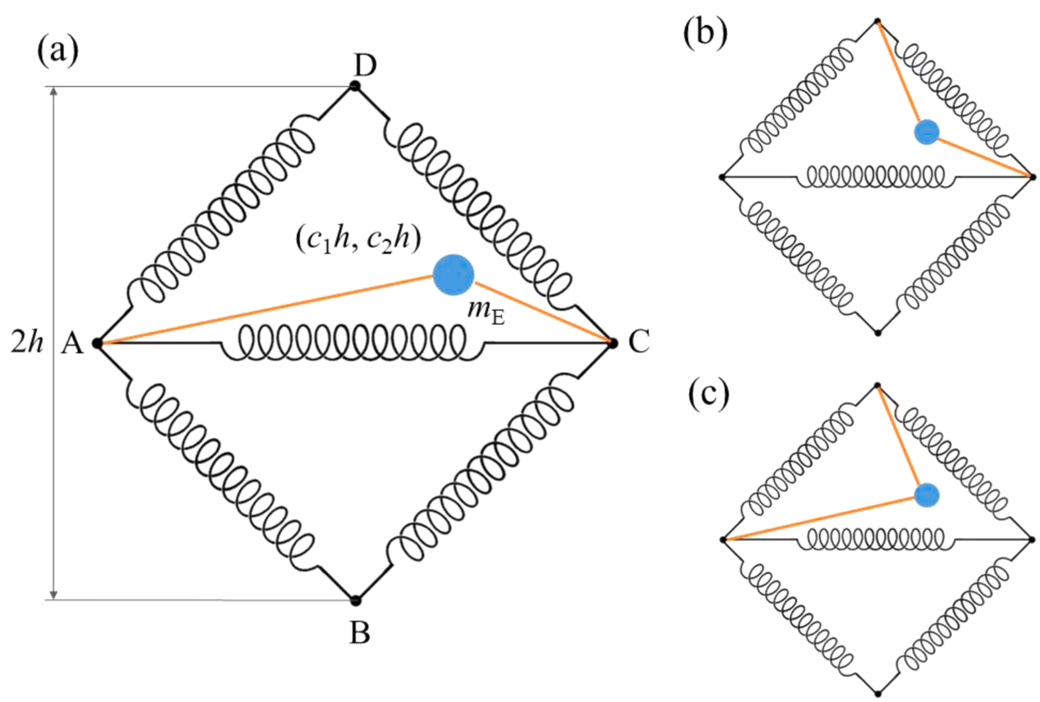

Fig. 1. Unit cell of the lumped-parameter model exhibiting Willis coupling. A coupling element composed of a concentrated mass point and two massless rigid rods can be placed on any pairs of lattice sites, and the mass position is parametrized as (c_1h, c_2h). Cases (a) AC, (b) AD and (c) CD are shown here.

Referring Fig. 1(a), placing the coordinate origin at the unit cell center, the boundary site positions of the unit cell are

$$\mathbf{x}^{\mathrm{A}} = \begin{pmatrix} -h \\ 0 \end{pmatrix}, \quad \mathbf{x}^{\mathrm{B}} = \begin{pmatrix} 0 \\ -h \end{pmatrix}, \quad \mathbf{x}^{\mathrm{C}} = \begin{pmatrix} h \\ 0 \end{pmatrix}, \quad \mathbf{x}^{\mathrm{D}} = \begin{pmatrix} 0 \\ h \end{pmatrix}, \tag{1}$$

respectively, while two nondimensional parameters c_1 and c_2 are introduced to specify the position of internal mass E,

$$\mathbf{x}^{\mathrm{E}} = h\begin{pmatrix} c_1 \\ c_2 \end{pmatrix}. \tag{2}$$

In the long wave limit $h/\lambda \to 0$, where λ is the wavelength, the displacement of the observable boundary sites can be approximated via Taylor's expansion in consistence with a macroscopic displacement field $\mathbf{u}$ and its gradient

$$\mathbf{u}^n = \mathbf{u}^0 + (\mathbf{u}\nabla)\cdot\mathbf{x}^n, \quad n \in \{A, B, C, D\}, \tag{3}$$

where $\mathbf{u}^0 = \mathbf{u}(\mathbf{0})$. Inside the cell, displacement of internal mass E can be derived from the rigid bar constraints. Let for example the coupling element attach on the AC sites (Fig. 1(a)), the infinitesimal displacements satisfy

$$\begin{cases} (\mathbf{u}^{\mathrm{E}} - \mathbf{u}^{\mathrm{A}})\cdot(\mathbf{x}^{\mathrm{E}} - \mathbf{x}^{\mathrm{A}}) = 0, \\ (\mathbf{u}^{\mathrm{E}} - \mathbf{u}^{\mathrm{C}})\cdot(\mathbf{x}^{\mathrm{E}} - \mathbf{x}^{\mathrm{C}}) = 0, \end{cases} \tag{4}$$

from which it can be solved that

$$\mathbf{u}^{\mathrm{E}} = \mathbf{u}^0 + h\begin{pmatrix} -c_1\dfrac{\partial u_1}{\partial x_1} - c_2\dfrac{\partial u_2}{\partial x_1} \\ -\dfrac{(1-c_1^2)}{c_2}\dfrac{\partial u_1}{\partial x_1} + c_1\dfrac{\partial u_2}{\partial x_1} \end{pmatrix}. \tag{5}$$

For time-harmonic excitation (with $e^{-i\omega t}$time convention), forces in the two bars $\mathbf{f}^{\mathrm{AE}}$ and $\mathbf{f}^{\mathrm{CE}}$ are induced and determined from the Newton's law,

$$\mathbf{f}^{\mathrm{EA}} + \mathbf{f}^{\mathrm{EC}} = -\omega^2 m_{\mathrm{E}}\mathbf{u}^{\mathrm{E}}. \tag{6}$$

Overall, the apparent stress and momentum density of the system can be defined by

$$\boldsymbol{\sigma} = \frac{1}{V}\sum_{n=A,B,C,D}\mathbf{f}^n \otimes \mathbf{x}^n, \qquad -i\omega\,\mathbf{p} = \frac{1}{V}\sum_{n=A,B,C,D}\mathbf{f}^n, \tag{7}$$

where $\mathbf{f}^{\mathrm{A}} \sim \mathbf{f}^{\mathrm{D}}$ are the forces exerted on boundary sites and V the unit cell volume. Since the coupling element and the background spring network act on the lattice sites additively, we solely consider the contribution of coupling element AC in Eq. (7) at this moment, thus it is simply that $\mathbf{f}^{\mathrm{B}} = \mathbf{f}^{\mathrm{D}} = 0$, $\mathbf{f}^{\mathrm{A}} = \mathbf{f}^{\mathrm{EA}}$ and $\mathbf{f}^{\mathrm{C}} = \mathbf{f}^{\mathrm{EC}}$. Using the above equations and taking the Voigt form of macroscopic stress, strain, momentum and velocity vectors

$$\boldsymbol{\sigma} = (\sigma_{11},\ \sigma_{22},\ \sigma_{12},\ \sigma_{21})^{\mathrm{T}},\ \boldsymbol{\varepsilon} = (u_{1,1},\ u_{2,2},\ u_{1,2},\ u_{2,1})^{\mathrm{T}},\ \mathbf{p} = (p_1,\ p_2)^{\mathrm{T}},\ \mathbf{v} = -i\omega(u_1^0,\ u_2^0)^{\mathrm{T}}, \tag{8}$$

the constitutive relation in Willis form can be derived for just the coupling element AC

$$\begin{pmatrix} \boldsymbol{\sigma} \\ \mathbf{p} \end{pmatrix} = \begin{pmatrix} \mathbf{C}^{\mathrm{AC}} & \mathbf{S}^{\mathrm{AC}} \\ \mathbf{D}^{\mathrm{AC}} & \rho^{\mathrm{AC}}\mathbf{I} \end{pmatrix}\begin{pmatrix} \boldsymbol{\varepsilon} \\ \mathbf{v} \end{pmatrix} = \begin{pmatrix} \mathbf{C}^{\mathrm{AC}} & -i\omega\boldsymbol{\Psi}^{\mathrm{AC}} \\ -i\omega(\boldsymbol{\Psi}^{\mathrm{AC}})^{\mathrm{T}} & \rho^{\mathrm{AC}}\mathbf{I} \end{pmatrix}\begin{pmatrix} \boldsymbol{\varepsilon} \\ \mathbf{v} \end{pmatrix}, \tag{9}$$

where $\rho^{\mathrm{AC}} = m_{\mathrm{E}}/(2h^2)$ and

$$\boldsymbol{\psi}^{\mathrm{AC}} = \begin{pmatrix} \psi_{111} & \psi_{112} \\ \psi_{221} & \psi_{222} \\ \psi_{121} & \psi_{122} \\ \psi_{211} & \psi_{212} \end{pmatrix} = \frac{-m_E}{2h}\begin{pmatrix} c_1 & \dfrac{1-c_1^2}{c_2} \\ 0 & 0 \\ 0 & 0 \\ c_2 & -c_1 \end{pmatrix}, \tag{10}$$

$$\mathbf{C}^{\mathrm{AC}} = -\frac{m_E\omega^2}{2}\begin{pmatrix} \dfrac{1-2c_1^2+c_1^4+c_1^2c_2^2}{c_2^2} & 0 & 0 & \dfrac{-c_1+c_1^3+c_1c_2^2}{c_2} \\ 0 & 0 & 0 & 0 \\ 0 & 0 & 0 & 0 \\ \dfrac{-c_1+c_1^3+c_1c_2^2}{c_2} & 0 & 0 & c_1^2+c_2^2 \end{pmatrix}. \tag{11}$$

It is seen that in absence of springs, the coupling element alone contributes not only to the coupling tensor but also to the stiffness tensor. Since no elastic element is included here, the constitutive relation is dynamically meaningful only and frequency dependent. The mechanism is that, under dynamical loading, the inertial force of the mass is dispatched through the bars to the lattice sites unevenly, and conversely relative motion of the lattice sites can also accelerate the internal mass even if their average is zero. In the original proposal, Milton [60] considered a pair of coupling elements with positive and negative masses respectively, and symmetrically placed on AC sites (i.e. $c_1 = 0$, $c_2 = \pm c$), with which the effect of coupling element on $\mathbf{C}$ tensor can be eliminated and only the $\mathbf{S}$ tensor is emphasized. This model will be revisited in the next section together with the wave propagation. However, we are more interested in the coupling tensor $\mathbf{S}$ induced by a coupling element, and as an idealized model, the effect on $\mathbf{C}$ can always be compensated by the background spring network. We focus mainly on the $\mathbf{S}$ ($\mathbf{D}$) tensor for now.

In general, the Willis coupling tensors are complex, and satisfy $\boldsymbol{D} = -\boldsymbol{S}^{\dagger}$ at fixed frequency and wave vector with superscript '$\dagger$' being the Hermitian conjugation, as required by causality and reciprocity [21]. Therein, the real part originates from the inter-cell effect, i.e. the finite phase speed across a unit cell, while the imaginary part reflects the intra-cell effect implying that the cell is locally asymmetric [22,23]. Here in this longwave-limit homogenization, the inter-cell effect is excluded and the coupling tensors are pure imaginary with $\boldsymbol{S} = \mathbf{D}^{\mathrm{T}}$ ($S_{ijk} = D_{kij}$). Moreover, it is noticed that the stress and strain are not symmetric because the angular momentum with respect to the cell center has to be balanced. Consequently, the current medium does not hold minor symmetry and differs with that Willis originally derived, in which ensemble average of local stress guarantees the symmetry of macroscopic stress [12]. It is possible to cancel the dependence of momentum on the local rotation by add another pair of coupling element with inversed positive / negative masses, as indicated by Milton [60], resulting in a medium with $\psi_{ijk} = \psi_{jik}$compatible the elasticity cloaking. However, model complexity and constraint on the attainable coupling parameters will be greatly increased.

Using the same procedure of Eqs. (4)-(7), for a coupling element attached on AD (Fig. 1(b)) or CD (Fig. 1(c)) sites, the effective coupling tensors can be also derived as

$$\boldsymbol{\psi}^{\mathrm{AD}} = \frac{-m_E}{2h(1+c_1-c_2)}\begin{pmatrix} (1+c_1)(1-c_2) & (1+c_1)c_1 \\ (1-c_2)c_2 & -(1+c_1)(1-c_2) \\ -c_1c_2 & (1+c_1)c_1 \\ (1-c_2)c_2 & c_1c_2 \end{pmatrix}, \tag{12}$$

$$\boldsymbol{\psi}^{\mathrm{CD}} = \frac{-m_E}{2h(1-c_1-c_2)}\begin{pmatrix} -(1-c_1)(1-c_2) & -(1-c_1)c_1 \\ -(1-c_2)c_2 & -(1-c_1)(1-c_2) \\ c_1c_2 & (1-c_1)c_1 \\ (1-c_2)c_2 & c_1c_2 \end{pmatrix}. \tag{13}$$

Corresponding expression of $\mathbf{C}$ tensors are quite lengthy and not listed here. The rest cases are dual to the previous ones and can be obtained by index and sign change. In particular, $\mathbf{C}^{\mathrm{BD}}$ and $\boldsymbol{\psi}^{\mathrm{BD}}$can be obtained by switching the indices 1 and 2 from $\mathbf{C}^{\mathrm{AC}}$ and $\boldsymbol{\psi}^{\mathrm{AC}}$, respectively. For case BC (AB), $\mathbf{C}^{\mathrm{BC(AB)}}$ is obtained by replacing (c_1, c_2) with (-c_1, -c_2) from those of case AD (CD), while $\boldsymbol{\psi}$ should be appended with an extra minus after the same operation since its order is odd. For instance,

$$\boldsymbol{\psi}^{\mathrm{BC}} = \frac{-m_E}{2h(1-c_1+c_2)} \begin{pmatrix} -(1-c_1)(1+c_2) & (1-c_1)c_1 \\ (1+c_2)c_2 & (1-c_1)(1+c_2) \\ c_1c_2 & (1-c_1)c_1 \\ (1+c_2)c_2 & -c_1c_2 \end{pmatrix}. \tag{14}$$

As a whole, the effective elastic matrix $\mathbf{C}^{\mathrm{b}}$ of the background spring network should be additively included in. Since the spring network, coupling units independently contribute to the final constitutive relation, theoretically it is possible to combine appropriate spring network and several coupling elements to achieve the needed effective stiffness and Willis coupling characteristics:

$$\begin{aligned} \mathbf{C} &= \mathbf{C}^{\mathrm{b}} + \left(\mathbf{C}^{\mathrm{AC}} + \mathbf{C}^{\mathrm{BC}} + \cdots\right), \\ \mathbf{S} &= -i\omega\left(\boldsymbol{\psi}^{\mathrm{AC}} + \boldsymbol{\psi}^{\mathrm{BC}} + \cdots\right). \end{aligned} \tag{15}$$

The effective density ρ is just the volume averaged total mass, including the masses on the lattice site for adjusting purpose.

3. Free wave propagation with particular material design

In this section, some unusual aspects of elastic wave propagation are examined and impacts of different **S** components are considered with particular design of the model. The results of homogenized Willis media will be compared with those of discrete models for validation.

Consider a plane wave travelling along x_1 direction $\hat{\mathbf{u}}e^{i(kx_1-\omega t)}$with $\hat{\mathbf{u}} = (\hat{u}_1,\ \hat{u}_2)^{\mathrm{T}}$being the complex amplitude and k the wave number. Using Eqs. (8) and (9) in the equation of momentum conservation $\nabla\cdot\boldsymbol{\sigma} = \dot{\mathbf{p}}$ yields

$$\begin{aligned} -C_{1111}k^2\hat{u}_1 + S_{111}\omega k\hat{u}_1 + S_{112}\omega k\hat{u}_2 &= D_{111}\omega k\hat{u}_1 + D_{121}\omega k\hat{u}_2 - \rho\omega^2\hat{u}_1, \\ -C_{2121}k^2\hat{u}_2 + S_{211}\omega k\hat{u}_1 + S_{212}\omega k\hat{u}_2 &= D_{211}\omega k\hat{u}_1 + D_{221}\omega k\hat{u}_2 - \rho\omega^2\hat{u}_2. \end{aligned} \tag{16}$$

Note that for simplicity components of **C** tensor related to tension-shear coupling, i.e. C_{ijkk}, are excluded, and we will intentionally avoid these parameters in the microstructural design. It is seen that there are only four $\boldsymbol{\psi}$components involved, while the remaining are irrelevant to waves traveling in x_1 direction. Eq. (16) gives two dispersion relations as,

$$k_{\mathrm{L,S}}^2 = \frac{1}{2}\omega^2\left(\frac{\rho}{C_{1111}} + \frac{\rho}{C_{2121}} + \frac{(\psi_{112}-\psi_{211})^2\omega^2 \mp R}{C_{1111}C_{2121}}\right), \tag{17}$$

where

$$R = \sqrt{\left(C_{2121}\rho + C_{1111}\rho + (\psi_{112}-\psi_{211})^2\omega^2\right)^2 - 4C_{1111}C_{2121}\rho^2}. \tag{18}$$

The expressions of eigenmode are lengthy and not suitable to list here. It is seen that for waves in x_1- direction, the involved Willis coupling parameters enter in the dispersion and eigenmodes only in the form of (ψ_{112} - ψ_{211}). It turns out that the wave is dispersive, meanwhile as long as $\psi_{112} \neq \psi_{211}$ the two eigen modes, $\hat{\mathbf{u}}_{\mathrm{L}}and\hat{\mathbf{u}}_{\mathrm{S}}$ are elliptical polarized with their long axes parallel or perpendicular to the wave vector. This wave behavior is essentially different with traditional elastic media, and here the subscripts L and S are labelled in analogy to the longitudinal and shear waves according to the long axes of the ellipse. The other two components, ψ_{111} and ψ_{212}, do not play a role in the dispersion and the eigenmodes, however, they do affect the resulting stress and velocity, and hence the elastic wave impedance as well.

Milton [60] suggested to introduce two coupling elements with mass m_{E} and m_{F} symmetrically attached on AC sites with locations respectively (0, c) and (0, -c), as shown in Fig. 2(a). In this situation, Eqs. (10) and (11) reduce to

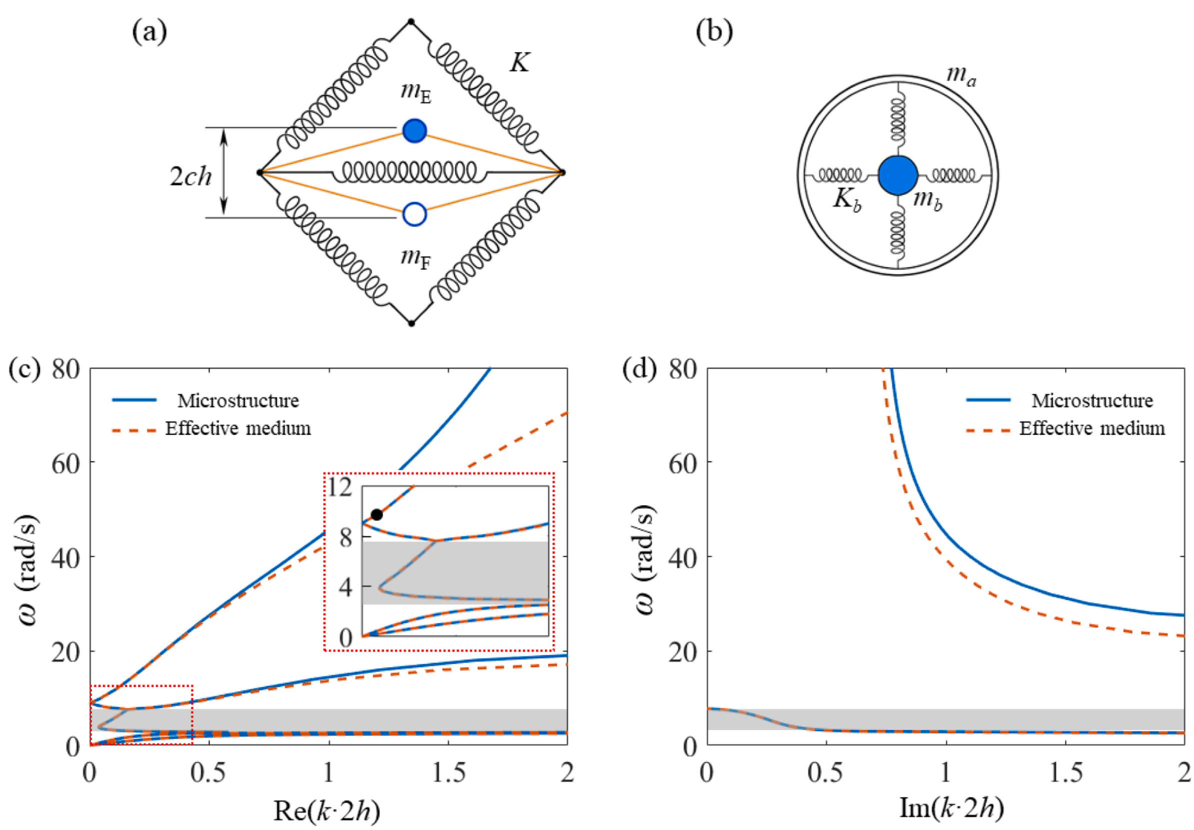

Fig. 2. (a) Original model of Milton [60] including two coupling elements with positive mass m_{E} and negative mass m_{F}, respectively. (b) Mass-in-mass unit realizing effective negative mass m_{F}. (c) Real part and (d) imaginary part of the complex band structure of the model. Grey shades indicate the band gap caused by the negative mass. The inset in (c) zooms band details around the low frequency and longwave regime, and the black point marks the frequency at which $m_E + m_F = \delta h^2$ holds.

$$\mathbf{C}^{AC} = -\frac{(m_E + m_F)\omega^2}{2}\begin{pmatrix} 1/c^2 & 0 & 0 & 0 \\ 0 & 0 & 0 & 0 \\ 0 & 0 & 0 & 0 \\ 0 & 0 & 0 & c^2 \end{pmatrix}, \quad \boldsymbol{\psi} = \begin{pmatrix} 0 & \psi_{112} \\ 0 & 0 \\ 0 & 0 \\ \psi_{211} & 0 \end{pmatrix} = \frac{m_F - m_E}{2h}\begin{pmatrix} 0 & 1/c \\ 0 & 0 \\ 0 & 0 \\ c & 0 \end{pmatrix}. \tag{19}$$

Assuming uniform spring constant K for the background spring network, the corresponding elastic tensor reads

$$\begin{pmatrix} \sigma_{11} \\ \sigma_{22} \\ \sigma_{12} \\ \sigma_{21} \end{pmatrix} = K\begin{pmatrix} 5/2 & 1/2 & 0 & 0 \\ 1/2 & 1/2 & 0 & 0 \\ 0 & 0 & 1/2 & 1/2 \\ 0 & 0 & 1/2 & 1/2 \end{pmatrix}\begin{pmatrix} u_{1,1} \\ u_{2,2} \\ u_{1,2} \\ u_{2,1} \end{pmatrix}. \tag{20}$$

Let the mass pair take a special form as $m_E = mh$ and $m_F = -mh + \delta h^2$with $m > 0$, so that $m_E + m_F = \delta h^2$ is a higher order small quantity and Eq. (19) implies that the coupling elements tend to produce exclusively the coupling tensor$\boldsymbol{\psi}$.

Practically, the negative mass can be achieved by a mass-in-mass component [2,15] as shown in Fig. 2(b), however, the effectiveness of negative mass will be frequency sensitive. In this scenario we have

$$m_F(\omega) = m_a + \frac{2K_b m_b}{2K_b - m_b\omega^2}, \tag{21}$$

where m_a, m_b and K_b are respectively the outer mass, hidden mass and the inner spring constant. Using material parameters of Eqs. (19) ~ (21) in Eq. (17), the complex band structure of the homogenized Willis medium is plotted by the dashed curves in Fig. 2(c) and Fig. 2(d), in which parameters $h = 0.1$m, $c = 0.2$, $m_E = 0.1$kg, $K = 170$N/m, $m_a = 0.009$kg, $m_b = 1$kg, $K_b = 4$N/m are used. The complex bands of the discrete model are also solved via Bloch wave analysis and plotted in the figure in solid lines for comparison. It is seen from band diagrams for both the real and imaginary part of the wavenumber that, the curves of homogenized model and discrete model are in good agreement for the wave number range $|2kh| < 1$, within which the homogenization is generally justified. At frequency $\omega = 9.4$ rad/s, the effective mass $m_F = -0.09$kg and $m_F = -m_E h + \delta h^2$ holds. In the figure, the gray shade indicates the band gap $\omega \in [2.8, 7.6]$ rad/s caused by the negative effective mass where the wave number is complex and the wave spatially attenuates in the material. In Fig. 2(d), an imaginary band also exists in high frequency since there is only one traveling mode at those frequencies. The Bloch wave analysis on Milton's model confirms that the longwave homogenization as well as the Willis coupling effect is quantitatively valid even when a feasible negative mass component is included in.

If we do not care the side effect of coupling elements on the stiffness tensor **C**, significant Willis coupling can still be achieved by keeping only one element with positive mass in the unit cell as shown in Fig. 3(a), since the lattice is asymmetric enough. Let $m_F = 0$, the corresponding dispersion curves are plotted in Fig. 3(b) with other parameters in the previous example unchanged. Because of the nonzero $(\psi_{112} - \psi_{211})$, the elliptical polarization of the two wave branches are also illustrated in the figure for $\omega = 9.4$rad/s. As anticipated, the comparison of the dispersion curves from homogenized medium and the discrete model also exhibits enough agreement. The unusual polarization in this model will be utilized in mode transfer by a sandwiched Willis material layer in Section 4.2.

On the other hand, if the Willis coupling presents but satisfying $\psi_{112} = \psi_{211}$, the waves propagating in x_1 direction are linearly polarized as purely longitudinal and shear like in a Cauchy medium. In order to construct such material, we can combine two coupling elements with $m_E = m_F = m$ symmetrically attached on CD and BC sites, with their mass positions parametrized as $(c_1, c_2) = (b, b)$ and $(c_1, c_2) = (b, -b)$, respectively, as shown in Fig. 3(a). Eqs. (13) and (14) then reduce to

$$\boldsymbol{\psi}^{CD} = \frac{-m}{2h(1-2b)}\begin{pmatrix} -(1-b)^2 & -(1-b)b \\ -(1-b)b & -(1-b)^2 \\ b^2 & (1-b)b \\ (1-b)b & b^2 \end{pmatrix}, \quad \boldsymbol{\psi}^{BC} = \frac{-m}{2h(1-2b)}\begin{pmatrix} -(1-b)^2 & (1-b)b \\ -(1-b)b & (1-b)^2 \\ -b^2 & (1-b)b \\ -(1-b)b & b^2 \end{pmatrix}. \tag{22}$$

The superposition of $\boldsymbol{\psi}^{CD}$and$\boldsymbol{\psi}^{BC}$cancels out the components $\psi_{112}$and ψ_{211}, and yields

$$\boldsymbol{\psi} = \begin{pmatrix} \psi_{111} & 0 \\ \psi_{221} & 0 \\ 0 & \psi_{122} \\ 0 & \psi_{212} \end{pmatrix} = \frac{-m}{h(1-2b)}\begin{pmatrix} -(1-b)^2 & 0 \\ -(1-b)b & 0 \\ 0 & (1-b)b \\ 0 & b^2 \end{pmatrix}. \tag{23}$$

The dispersion curves of the model in Fig. 4(a) are exemplified in Fig. 4(b) with the microstructural parameters $h = 0.1$m, $b = 0.2$, $K = 170$N/m, $m_E = m_F = 0.05$kg. Again, curves of the homogenized model approximate those of the lattice model very well at longwave range, and the polarization is of pure longitudinal and shear wave as expected. The model in Fig. 4(a) will be used in section 4.1 in demonstrating the asymmetric phase factor of wave reflection.

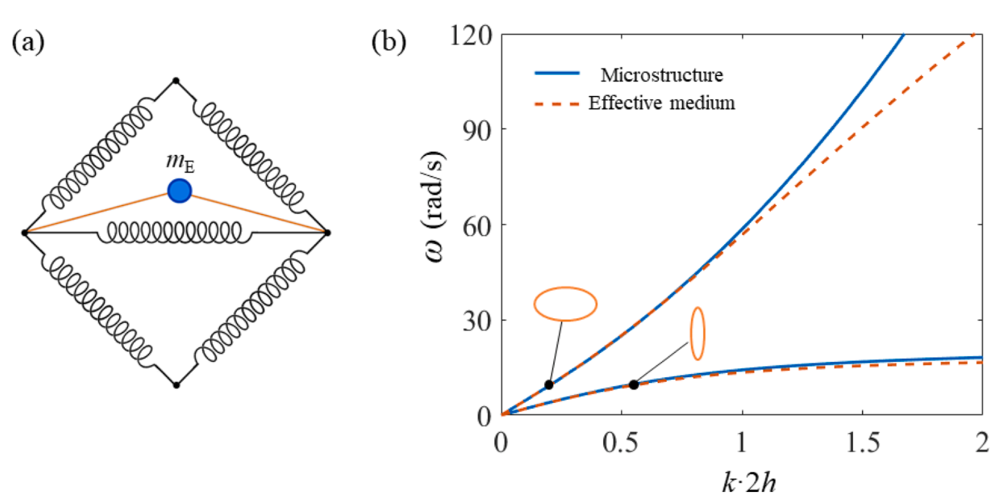

Fig. 3. (a) The Willis material model using a single coupling element with positive mass m_E. (b) Comparison of dispersion curves obtained from the homogenized and the discrete model, elliptically polarized modes of the two branches are exemplified.

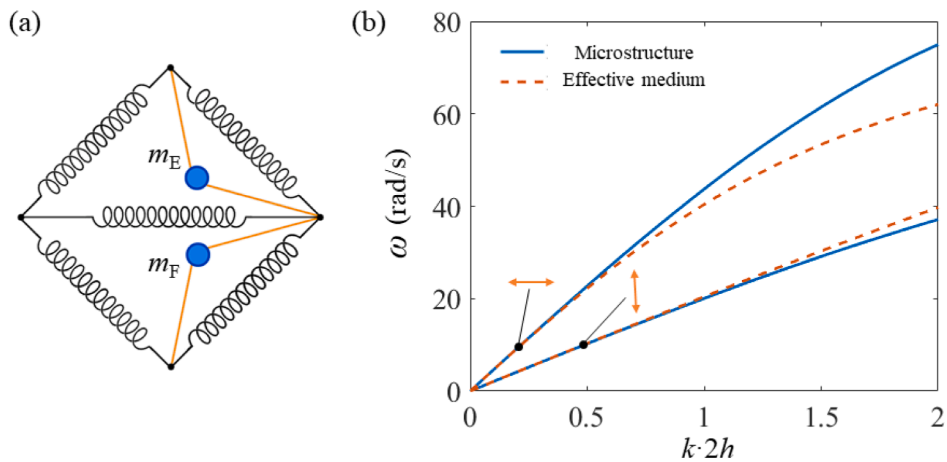

Fig. 4. (a) The unit cell with two coupling elements symmetrically attached on CD and BC sites, the model possesses Willis coupling but the polarization remains traditional. (b) Comparison of the dispersion curves obtained from the homogenized and discrete model, linearly polarized modes are exemplified.

4. Wave transmission across a sandwiched willis layer

Having been acquainted and confirmed by free wave properties, we consider in this section the wave transmission across a layer of the proposed Willis material model. With specifically designed lattice layers with appropriate coupling components, wave functionalities of asymmetric reflection and mode conversion are exemplified to verify the design capability as well as the theoretical formulation related to the proposed Willis material model.

As sketched in Fig. 5, the Willis material layer with thickness d is sandwiched by two semi-infinite traditional elastic media. The Willis layer is characterized by stiffness tensor $\mathbf{C}$, coupling tensor $\boldsymbol{\psi}$ and density ρ, and the Cauchy domain on both sides are characterized by $\mathbf{C}^0$ and ρ^0. We consider incident waves normal to the layer, and assume that all the materials have their principal axes aligned with coordinate direction, so that the incident, reflected and transmitted waves are purely longitudinal or shear. The waves in the layer could be elliptically or linearly polarized, depending on the microstructural setup as discussed in the previous section. The displacement field inside the Willis layer is superposition of four waves

$$\mathbf{u} = \mathbf{P}_{\mathrm{L}}\left(Ae^{ik_{\mathrm{L}}x} + Be^{-ik_{\mathrm{L}}x}\right) + \mathbf{P}_{\mathrm{S}}\left(Ce^{ik_{\mathrm{S}}x} + De^{-ik_{\mathrm{S}}x}\right), \tag{24}$$

where $\mathbf{P}_{\mathrm{L}} = (P_{\mathrm{L1}}, P_{\mathrm{L2}})^{\mathrm{T}}$ and $\mathbf{P}_{\mathrm{S}} = (P_{\mathrm{S1}}, P_{\mathrm{S2}})^{\mathrm{T}}$ are the polarization vectors, which are normalized to be unitary, for the two wave modes with wave number k_{L} and k_{S}, respectively. Constants $A \sim D$ are the amplitude coefficients to be determined. The envisaged transmission and reflection coefficients t_{L}, t_{S} and r_{L}, r_{S} can be determined via the transfer matrix method (TMM). Generally, a scattering matrix $\mathbf{S}$ can be defined to link the involved waves at the two ports of the Willis layer (Fig. 5),

$$\begin{pmatrix} t_{\mathrm{L}}e^{-ik_{\mathrm{L}}d} \\ 0 \\ t_{\mathrm{S}}e^{-ik_{\mathrm{S}}d} \\ 0 \end{pmatrix} = \mathbf{S}\begin{pmatrix} i_{\mathrm{L}} \\ r_{\mathrm{L}} \\ i_{\mathrm{S}} \\ r_{\mathrm{S}} \end{pmatrix}, \tag{25}$$

by which t_{L}, t_{S}, r_{L}, and r_{S} can be solved for two cases, i.e., $(i_{\mathrm{L}}, i_{\mathrm{S}}) = (1, 0)$ or $(0, 1)$ corresponding to longitudinal or shear wave incidence, respectively. The scattering matrix can be expressed as

$$\mathbf{S} = \mathbf{M}_0^{-1}\mathbf{T}\mathbf{M}_0,\ \mathbf{T} = \mathbf{M}\mathbf{N}(d)\mathbf{M}^{-1}, \tag{26}$$

where $\mathbf{T}$ is the transfer matrix of the Willis layer, $\mathbf{M}_0$ and $\mathbf{M}$ are impedance matrices of the background medium and Willis medium, respectively, and $\mathbf{N}(d)$ is the spatial phase matrix across the layer. Derivation of these matrices are detailed in the Appendix. Base on the TMM in this scenario, we demonstrate in the following two examples showing the effect of Willis coupling on the wave transmission, in conjunction with appropriate design of the lattice model.

4.1. Asymmetric reflection in phase by the willis layer

It has been observed in acoustic waves [33,39] and flexural waves [40] that passive Willis media could induce asymmetric reflection. The similar phenomenon also exists in elastic waves with the proposed Willis material model. The transmission and reflection coefficients ruled by Eq. (25) is in general difficult to be expressed analytically. Here, we

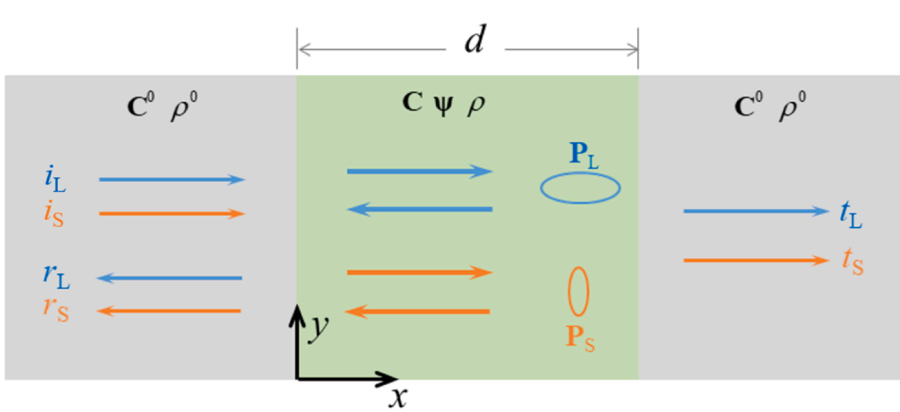

Fig. 5. Problem setup for wave transmission through a Willis medium layer of thickness d. The incident, reflected and transmitted waves may contain two different modes identified by different colors.

concentrate on a simplified case with $\psi_{112} = \psi_{211} = 0$, hence the two eigenmodes are polarized like Cauchy medium, i.e. $\mathbf{P}_L = (1, 0)^T$and $\mathbf{P}_S = (0, 1)^T$, the expression will be greatly simplified. In case of longitudinal wave incidence, all wave excited in the three domains are all longitudinal, and the transmission and reflection coefficients are

$$t_L = \frac{4\bar{k}_{L0}\bar{k}_L e^{idk_L}}{2\bar{k}_{L0}\bar{k}_L(1+e^{2idk_L}) + (\bar{k}_{L0}^2 + \bar{k}_L^2 + \omega^4\psi_{111}^2)(1-e^{2idk_L})} \tag{27}$$

$$r_L = \frac{(1-e^{2idk_L})(\bar{k}_{L0}^2 - \bar{k}_L^2 - \omega^4\psi_{111}^2 - 2i\bar{k}_{L0}\omega^2\psi_{111})}{2\bar{k}_{L0}\bar{k}_L(1+e^{2idk_L}) + (\bar{k}_{L0}^2 + \bar{k}_L^2 + \omega^4\psi_{111}^2)(1-e^{2idk_L})} \tag{28}$$

where $\bar{k}_L = C_{1111}k_L$ and $\bar{k}_{L0} = C_{1111}^0 k_{L0}$ with k_{L0}being the longitudinal wave number in Cauchy medium. It is obvious that except the usual stiffness and density, coupling parameter ψ_{111} could be employed to tune the transmission and reflection. In particular, from Eq. (28), if we do not want reflection happens, the first or the second bracket in the numerator should be zero. The former yields $2d = n\lambda_L$, where λ_L is the wave length. This is the same condition for full transmission as in ordinary media. The second bracket is related to the impedance matching. However, if ψ_{111} has a nonzero value, there is always an imaginary part preventing the perfect impedance matching. Moreover, if the incident wave is from another side or equivalently the Willis layer is reversed, the coupling parameter ψ_{111} has to reverse the sign since it is a third order tensor. Upon such reversion, the transmission (Eq. (27)) keeps unchanged while the reflection coefficient (Eq. (28)) alters, implying different phases for the reflected waves.

The same effects also apply for the case of shear wave incidence, for which the coupling coefficient ψ_{212} takes in charge. Namely, the corresponding reflection coefficient is

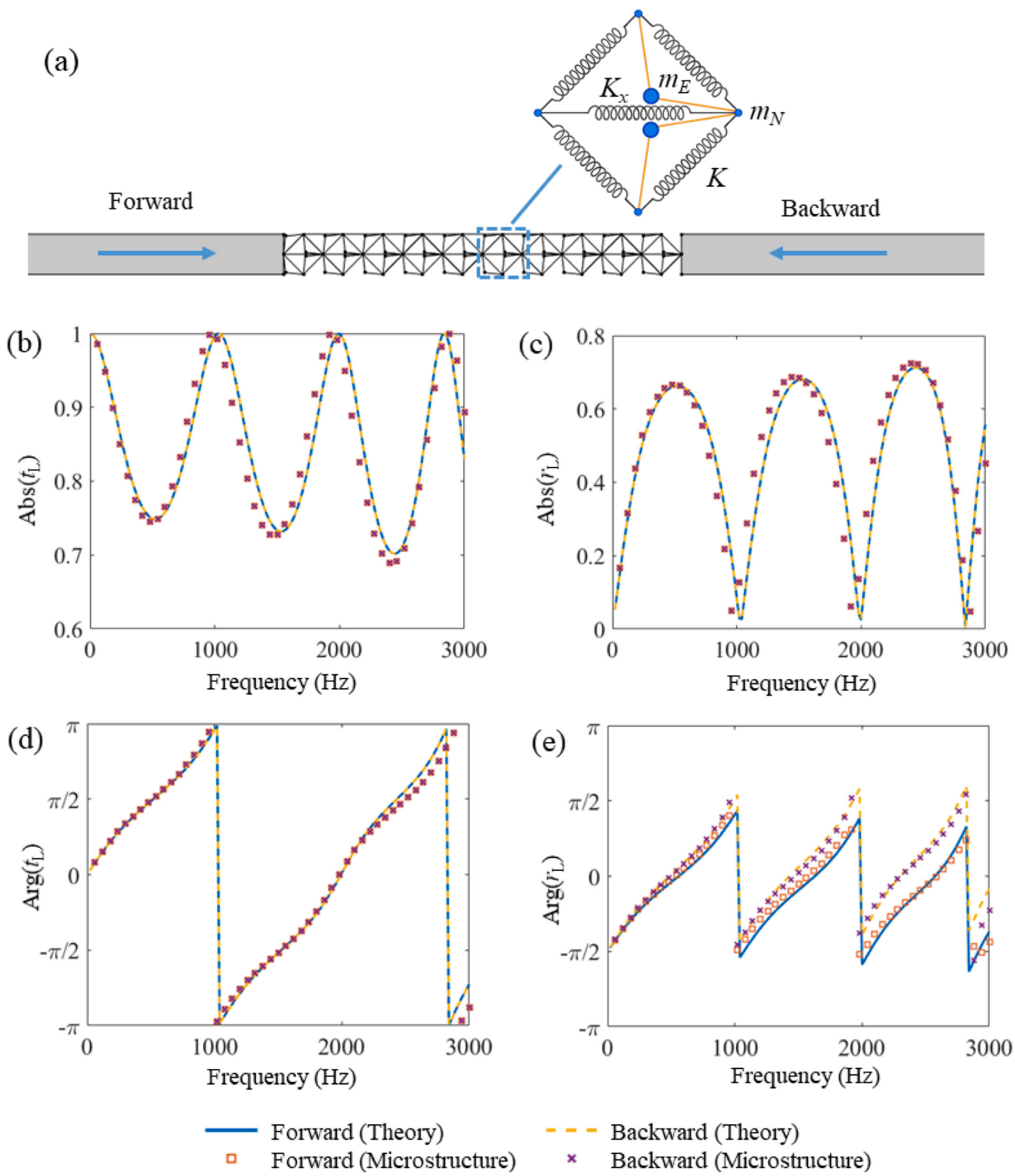

Fig. 6. (a) Simulated model of longitudinal wave transmission across a Willis material layer in case of forward or backward incidence. Amplitudes of (b) transmission and (c) reflection coefficients; phase of (d) transmission and (e) reflection coefficients as functions of frequency. Curves are graphed via TMM with effective parameters, while scattered dots are obtained by FEM simulation.

$$r_S = \frac{(1-e^{2idk_S})\left(\overline{k}_{S0}^2 - \overline{k}_S^2 - \omega^4\psi_{212}^2 - 2i\overline{k}_{S0}\omega^2\psi_{212}\right)}{2\overline{k}_{S0}\overline{k}_S(1+e^{2idk_S}) + \left(\overline{k}_{S0}^2 + \overline{k}_S^2 + \omega^4\psi_{212}^2\right)(1-e^{2idk_S})} \tag{29}$$

where $\overline{k}_S = C_{2121}k_S$ and $\overline{k}_{S0} = C^0_{2121}k_{S0}$ with k_{S0} being the shear wave number in Cauchy medium.

On the basis of theoretical analysis, we verified mentioned asymmetric reflection numerically. For the longitudinal wave incidence, the simulation setup is shown in Fig. 6(a). The polymethyl methacrylate (PMMA) is used as the isotropic background medium with Young's modulus E^0 =5.35GPa, Poisson's ratio $\nu^0 = 0.35$ and density $\rho^0 = 1180\text{kg/m}^3$. The Willis material layer with $d = 0.5$m is composed of 10 unit cells. Conforming with $\psi_{112} = \psi_{211} = 0$ as required by the theory, a unit cell similar with that in Fig. 4 is adopted. In order to increase the tunability of the effective Willis properties, the constants of the spring network are allowed to have different values (K_x and K), in addition, extra point masses m_N are attached on the lattice sites, as depicted in Fig. 6(a). The microstructural parameters used in calculation are $h = 0.025$m, $K = 1 \times 10^9$ N/m, $K_x = 0.5 \times 10^9$ N/m, $m_E = 0.8$kg, $m_N = 0.1$kg. Since for longitudinal wave the effective coupling parameter ψ_{111} is crucial, the internal masses are placed near the cell center, i.e. $b = 0.1$. It is evaluated from Eq.(23) that $\psi_{111} = 32.4$ kg/m^2, and the relevant effective modulus and density are $C_{1111} = (1.5 \times 10^9 - 0.855\omega^2)$ Pa, $\rho = 1360$ kg/m^3 for the Willis layer. Note that modulus C_{1111} is frequency dependent due to the contribution of coupling element. Here and after, finite element method (FEM) simulation in frequency domain is carried out via COMSOL software. The background continuum is modeled by solid element while the springs and rigid rods are modeled by truss elements, and the Young's modulus of rods is set as very large (equivalent to $K = 1 \times 10^{12}$ N/m). Periodic condition is applied in the vertical direction, and the perfect match layers (PMLs) are set on the left and right ends. The transmission and reflection coefficients are estimated by retrieving displacements at 4 points mimicking standard 4-microphone method [52].

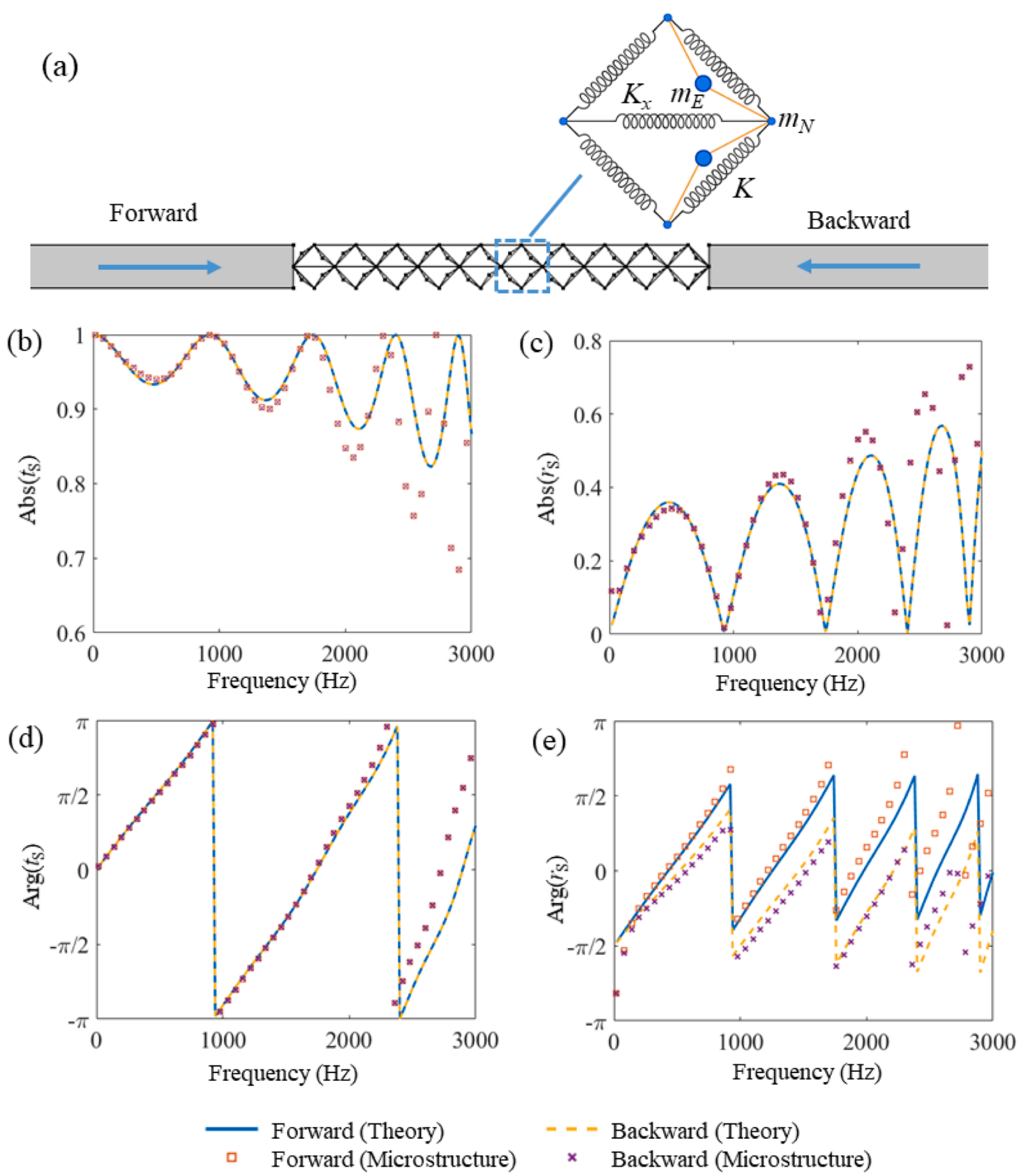

Fig. 7. (a) Simulated model of shear wave transmission across a Willis layer in case of forward or backward incidence. Amplitudes of (b) transmission and (c) reflection coefficients; phase of (d) transmission and (e) reflection coefficients as functions of frequency. Curves are graphed via TMM with effective parameters, while scattered dots are obtained by FEM simulation.

Consider the forward and backward longitudinal wave incidence, i.e. the wave impinging respectively from the left and right side of the layer, the transmission and reflection detail are calculated and compared in Fig. 6(b)-(e) within the frequency range 0–3000Hz. The sweeping step length is 20 Hz. In the figure, curves are graphed from Eqs. (27) and (28) using effective parameters, while scattered dots are evaluated from direct simulation of the mixed model containing the continuum background media and the discrete latticed layer shown in Fig. 6(a). Compare Fig. 6(b) and 6(d), it is observed that the amplitudes and phases of transmitted waves are both the same for forward incidence and backward incidence. Conversely for reflected waves, Fig. 6(c) and 6(e) show that the amplitudes are the same, but their phases are different for the two direction of incidence, confirming the phase asymmetry in the reflection. The good agreement of predictions from the effective and discrete model further verifies the Willis material design and homogenization in previous sections.

As for case of shear wave incidence, coupling parameter ψ_{212} should be emphasized, according to Eq. (23) it is reasonable to put the internal masses near the cell margin, e.g. $b = 0.4$, as depicted in Fig. 7(a). Other microstructural parameters are chosen as $K = 2 \times 10^9$ N/m, K_x= 0.5×10^9 N/m, $m_E = 0.6$kg, $m_N = 0.2$kg, with which the induced relevant effective properties of the Willis layer can be evaluated as $\psi_{212} = -19.2$ kg/m^2, $C_{2121} = (1 \times 10^9 - 1.298\omega^2)$ Pa, $\rho = 1120$ kg/m^3. With these in hand, the transmission and reflection behavior for forward and backward shear wave incidence are also calculated and displayed in Fig. 7 (b)-(e). Again, pronounced asymmetry in phase for the reflected shear wave is observed both by the theoretical and FEM simulation. Compared with the longitudinal wave, it is seen that the discrepancy between the homogenized and real model increases as frequency goes up. This is due to the shorter wavelength of the shear wave, for which the homogenization based on first order expansion deteriorates faster.

4.2. elastic wave transmodal layer by willis coupling

As an application of this Willis material model, we illustrate in this subsection an example that converts elastic wave efficiently from longitudinal mode to shear mode. Kweun et al. [61] designed an metamaterial layer with slits to couple and convert two wave modes to each other. As hinted by Fig. 3, a Willis material layer supporting elliptical wave polarization obviously also couples two wave modes on both sides, so it is intuitive that it may achieve the same function.

The problem is defined as, given the background medium, layer thickness and operating frequency, to find an optimal set of Willis material parameters achieving the maximum conversion efficiency of wave mode. We consider for example the longitudinal-to-shear wave conversion. The mode converting efficiency to be maximized can be quantified by normalized longitudinal-to-shear mode transmission power [61],

$$T_{\mathrm{S}} = \sqrt{\frac{C^0_{2121}}{C^0_{1111}}}|t_{\mathrm{S}}|^2. \tag{30}$$

Similarly, powers of other scattered wave parts are defined as

$$T_{\mathrm{L}} = |t_{\mathrm{L}}|^2, \quad R_{\mathrm{S}} = \sqrt{\frac{C^0_{2121}}{C^0_{1111}}}|r_{\mathrm{S}}|^2, \quad R_{\mathrm{L}} = |r_{\mathrm{L}}|^2. \tag{31}$$

As an example, we use also the PMMA as the background medium, fix the layer thickness $d = 1.3$m and set the frequency $f = 2000$Hz. In the calculation of t_{S} in x_1 direction by Eq. (25), it is noticed that four coupling parameters ψ_{111}, ψ_{112}, ψ_{211} and ψ_{212} enter the scattering matrix **S**, other related parameters are C_{1111}, C_{2121} and ρ. For simplicity, we choose five parameters (C_{1111}, C_{2121}, ψ_{111}, ψ_{112}, ρ) for the Willis layer to be optimized to maximize the longitudinal-to-shear transmission power T_{S}. Employing genetic optimization algorithm, a set of optimized parameters is figured out and listed in Table 1. With these parameters, transmission powers for each reflected and transmitted wave calculated from Eqs. (25), (30) and (31) are reported in the first row of Table 2. Further inspection reveals that the optimized parameters have the following characteristics: (a) the polarization ellipses of the two modes overlap and only differ in phase; (b) the induced wavenumber k_{S} and k_{L} satisfy $d(k_{\mathrm{S}} - k_{\mathrm{L}})=\pi$. Ref. [62] derived a theoretical bound for the longitudinal-to-shear converting efficiency $T_{\mathrm{SBound}} = 4\xi/(1+\xi)^2$ with $\xi = [(1-2\nu^0)/(2-2\nu^0)]^{1/2}$. For the current PMMA material $T_{\mathrm{SBound}} =$ 87.6%, the optimized parameter gives $T_{\mathrm{S}} = 86.2\%$ which is very close to this bound.

Since the optimization gives $\psi_{111} = 0$, we use the cell configuration in Fig. 3(a) to approximate the required effective material properties, which has a coupling tensor as Eq. (19). To increase design freedom, the model is allowed to have different spring constants (K_x and K) and extra point masses m_N on the lattice sites, as depicted in Fig. 8(b). Referring to Eq. (19), we choose $c = -0.2$ so that $\psi_{211} = 0.04\psi_{112}$ is sufficiently small, and set the cell size $h = 0.025$m thus $2k_S h = 0.48 < 1$ so that the homogenization is justified. Other parameters are determined as $K = 4.68\times10^9$N/m, K_x=0.345×10^9N/m, m_{E}=0.3512kg, m_{N}=0.9185kg, with which the effective properties at the operating frequency are listed in the second row of Table 1.

We carried out FEM simulations to verify the proposed transmodal Willis layer. In Fig. 8(a), a long strip composed of PMMA on both sides and continuum Willis layer with the effective properties in Table 1 in the middle is first simulated. PMLs on both ends and periodic condition on the up and bottom edges are enforced to mimic infiniteness of the domain. Upon a longitudinal wave incidence, Fig. 8(a) shows the simulated fields of displacement components u_1 and u_2, indicating in this case the longitudinal and shear wave contents, respectively. It is seen that u_1 field and u_2 field are dominating respectively in front of and behind the layer, which proves high-efficient mode conversion. The longitudinal and shear waves can also be recognized by their wavelength in the fields. Quantitatively, transmission and reflection powers are estimated by the standard 4-microphone method [52]. Results are listed in the second row of Table 2. In particular, the retrieved $T_{\mathrm{S}} =$ 86.1% agrees very well with the TMM prediction, serving also a calibration for the FEM analysis.

Next, we replace the Willis layer by the designed lattice material with 26 cells, and the same simulated results are presented in Fig. 8(b). It is found that all the fields of displacement components inside the three sections of the domain match the results of effective continuum layer very well. The trajectories of six lattice nodes are drawn in the inset, showing the transfer process from horizontal displacement to vertical displacement. The retrieved transmission and reflection powers are

Table 2
Transmission and reflection powers via theoretical and FEM calculation.

	T_S	T_L	R_S	R_L
theoretical TMM	86.2%	1.6%	0.8%	11.5%
homogenized FEM	86.1%	1.6%	0.2%	12%
lattice model FEM	87%	2%	1.4%	9.5%

Table 1
Desired and approximated material properties of the Willis layer.

	C_{1111}(GPa)	C_{2121}(GPa)	ψ_{111}(kg/m^2)	ψ_{112}(kg/m^2)	ψ_{211}(kg/m^2)	ρ(kg/m^3)
optimized	2.3	2.3	0	35.1	/	1016
effective	2.3	2.3	0	35.12	1.4	1015.8

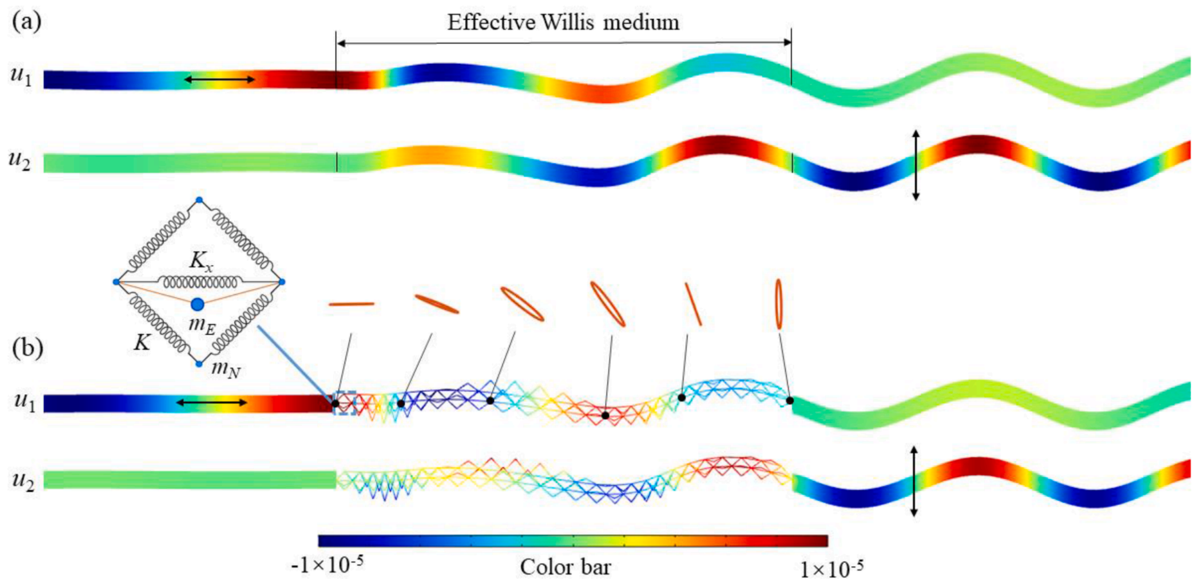

Fig. 8. FEM simulation of the transmodal Willis layer under longitudinal wave incidence from the left. (a) deformation and displacement contour of the model using continuum layer with optimized properties; (b) deformation and displacement contour with a latticed layer realizing targeted effective properties. The latticed layer is composed of 26 unit cells. Trajectories of six lattice sites are selectively drawn to show the transfer sequence of the polarization.

listed in the third row of Table 2. It is noticed from the table that $T_S =$ 87%, which is slightly higher than the theoretical value, is obtained using the discrete lattice. This might be attributed to the discrepancy of the homogenization and the real lattice at finite wavelength.

5. Conclusions

We studied a two-dimensional lumped-parameter model which can be homogenized in the longwave limit as elastic media effectively exhibiting Willis coupling. The model was originally proposed by Milton [60] and is extended here by allowing the coupling elements to traverse in the unit cell, and it is proved that different components of the coupling coefficient can be generated. By combination of several coupling elements in a cell it is possible to achieve a desired pattern of Willis coupling tensor.

The effective Willis coupling and designability of the model are validated via free wave analysis, with which the dispersion and tunable wave polarization are confirmed via several typical designs of models. In particular, the effective parameters can characterize the complex band structure in locally resonant band gaps. We further studied the wave transmission in a sandwiched Willis material layer, by which two elastic wave functionalities, i.e. the asymmetric reflection of elastic wave and the longitudinal-to-shear wave conversion, are enlightened and realized with appropriate material design.

Although the Willis material proposed in this work is more of a conceptual model, and whether arbitrary effective properties can be attained is not pursued in depth, it is enlightening and may shed light on more practical material design as well as the elastic wave manipulation via Willis media.

CRediT authorship contribution statement

Hongfei Qu: Methodology, Investigation, Validation, Software, Writing – original draft. **Xiaoning Liu:** Supervision, Conceptualization, Resources, Writing – review & editing. **Gengkai Hu:** Supervision, Writing – review & editing.

Declaration of Competing Interest

The authors declare that they have no known competing financial interests or personal relationships that could have appeared to influence the work reported in this paper.

Acknowledgements

This work was supported by the National Natural Science Foundation of China (Grant No. 11972080 and 11632003).

Appendix

Define a vector function of field variables relevant to the interface continuity, $\mathbf{f}(x) = (v_1 \quad v_2 \quad \sigma_{11} \quad \sigma_{21})^{\mathrm{T}}$, consider the assumed wave field Eq. (24) and the constitutive relation Eq. (9), inside the Willis layer the $\mathbf{f}$ function can be related to the amplitude vector $\mathbf{A} = (A\ B\ C\ D)^{\mathrm{T}}$ as

$$\mathbf{f}(x) = \mathbf{MN}(x)\mathbf{A}, \tag{A1}$$

where

$$\mathbf{N}(x) = \mathrm{diag}\left[e^{ik_L x} \quad e^{-ik_L x} \quad e^{ik_S x} \quad e^{-ik_S x} \right], \tag{A2}$$

and components of the $\mathbf{M}$ matrix read

$$\begin{aligned}
&M_{11}=M_{12}=-i\omega P_{L1},\quad M_{13}=M_{14}=-i\omega P_{S1},\\
&M_{21}=M_{22}=-i\omega P_{L2},\quad M_{23}=M_{24}=-i\omega P_{S2},\\
&M_{31}=ik_L C_{1111}P_{L1}-\omega^2\psi_{111}P_{L1}-\omega^2\psi_{112}P_{L2},\\
&M_{32}=-ik_L C_{1111}P_{L1}-\omega^2\psi_{111}P_{L1}-\omega^2\psi_{112}P_{L2},\\
&M_{33}=ik_S C_{1111}P_{S1}-\omega^2\psi_{111}P_{S1}-\omega^2\psi_{112}P_{S2},\\
&M_{34}=-ik_S C_{1111}P_{S1}-\omega^2\psi_{111}P_{S1}-\omega^2\psi_{112}P_{S2},\\
&M_{41}=ik_L C_{2121}P_{L2}-\omega^2\psi_{211}P_{L1}-\omega^2\psi_{212}P_{L2},\\
&M_{42}=-ik_L C_{2121}P_{L2}-\omega^2\psi_{211}P_{L1}-\omega^2\psi_{212}P_{L2},\\
&M_{43}=ik_S C_{2121}P_{S2}-\omega^2\psi_{211}P_{S1}-\omega^2\psi_{212}P_{S2},\\
&M_{44}=-ik_S C_{2121}P_{S2}-\omega^2\psi_{211}P_{S1}-\omega^2\psi_{212}P_{S2}.
\end{aligned}\tag{A3}$$

The following relation holds at both ends of the Willis layer

$$\mathbf{A}=\mathbf{N}(0)^{-1}\mathbf{M}^{-1}\mathbf{f}(0_+)=\mathbf{N}(d)^{-1}\mathbf{M}^{-1}\mathbf{f}(d_-),\tag{A4}$$

with which the transfer matrix relating the state vectors across the layer, $\mathbf{f}(d_-)=\mathbf{T}\mathbf{f}(0_+)$, can be defined as

$$\mathbf{T}=\mathbf{M}\mathbf{N}(d)\mathbf{M}^{-1}.\tag{A5}$$

On the Cauchy media side, state vectors are expressed as

$$\mathbf{f}(0_-)=\mathbf{M}_0\begin{pmatrix}u_{in}\\ r_L\\ v_{in}\\ r_S\end{pmatrix},\quad \mathbf{f}(d_+)=\mathbf{M}_0\begin{pmatrix}t_L e^{-ik_L d}\\ 0\\ t_S e^{-ik_S d}\\ 0\end{pmatrix},\tag{A6}$$

where

$$\mathbf{M}_0=i\omega\begin{bmatrix}-1&-1&0&0\\ 0&0&-1&-1\\ \sqrt{\rho^0C^0_{1111}}&-\sqrt{\rho^0C^0_{1111}}&0&0\\ 0&0&\sqrt{\rho^0C^0_{2121}}&-\sqrt{\rho^0C^0_{2121}}\end{bmatrix}.\tag{A7}$$

Enforce the continuity conditions of the fields at the two interfaces of the layer, $\mathbf{f}(0_-)=\mathbf{f}(0_+)$ and $\mathbf{f}(d_-)=\mathbf{f}(d_+)$, Eqs. (25) and (26) in the main text are obtained.

References

[1] Fang N, Xi D, Xu J, Ambati M, Srituravanich W, Sun C, Zhang X. Ultrasonic metamaterials with negative modulus. Nat Mater 2006;5(6):452–6.
[2] Liu ZY, Zhang XX, Mao YW, Zhu YY, Yang ZY, Chan CT, Sheng P. Locally resonant sonic materials. Science 2000;289(5485):1734–6.
[3] Torrent D, Sánchez-Dehesa J. Anisotropic mass density by two-dimensional acoustic metamaterials. New J Phys 2008;10(2):023004.
[4] Zhang HK, Chen Y, Liu XN, Hu GK. An asymmetric elastic metamaterial model for elastic wave cloaking. J Mech Phys Solids 2020;135:103796.
[5] Scheibner C, Souslov A, Banerjee D, Surówka P, Irvine WTM, Vitelli V. Odd elasticity. Nat Phys 2020;16(4):475–80.
[6] Zhang XD, Liu ZY. Negative refraction of acoustic waves in two-dimensional phononic crystals. Appl Phys Lett 2004;85(2):341–3.
[7] Zhu R, Liu XN, Hu GK, Sun CT, Huang GL. Negative refraction of elastic waves at the deep-subwavelength scale in a single-phase metamaterial. Nat Commun 2014;5 (1):1–8.
[8] Ambati M, Fang N, Sun C, Zhang X. Surface resonant states and superlensing in acoustic metamaterials. Phys Rev B 2007;75(19):195447.
[9] Zhang HK, Zhou XM, Hu GK. Shape-adaptable hyperlens for acoustic magnifying imaging. Appl Phys Lett 2016;109(22):224103.
[10] Chen HY, Chan CT. Acoustic cloaking in three dimensions using acoustic metamaterials. Appl Phys Lett 2007;91(18):183518.
[11] Chen Y, Liu XN, Hu GK. Latticed pentamode acoustic cloak. Sci Rep 2015;5:15745.
[12] Willis JR. Variational principles for dynamic problems for inhomogeneous elastic media. Wave Motion 1981;3(1):1–11.
[13] Milton GW, Briane M, Willis JR. On cloaking for elasticity and physical equations with a transformation invariant form. New J Phys 2006;8(10):248.
[14] Norris AN, Shuvalov AL. Elastic cloaking theory. Wave Motion 2011;48(6):525–38.
[15] Milton GW, Willis JR. On modifications of Newton's second law and linear continuum elastodynamics. P Roy Soc A 2007;463(2079):855–80.
[16] Willis JR. Effective constitutive relations for waves in composites and metamaterials. P Roy Soc A 2011;467(2131):1865–79.
[17] Nemat-Nasser S, Srivastava A. Overall dynamic constitutive relations of layered elastic composites. J Mech Phys Solids 2011;59(10):1953–65.
[18] Shuvalov AL, Kutsenko AA, Norris AN, Poncelet O. Effective Willis constitutive equations for periodically stratified anisotropic elastic media. P Roy Soc A 2011; 467(2130):1749–69.
[19] Norris AN, Shuvalov AL, Kutsenko AA. Analytical formulation of three-dimensional dynamic homogenization for periodic elastic systems. P Roy Soc A 2012;468 (2142):1629–51.
[20] Nassar H, He QC, Auffray N. Willis elastodynamic homogenization theory revisited for periodic media. J Mech Phys Solids 2015;77:158–78.
[21] Muhlestein MB, Sieck CF, Alu A, Haberman MR. Reciprocity, passivity and causality in Willis materials. P Roy Soc A 2016;472(2194):20160604.
[22] Sieck F, Alù A, Haberman MR. Origins of Willis coupling and acoustic bianisotropy in acoustic metamaterials through source-driven homogenization. Phys Rev B 2017;96(10):104303.
[23] Alù A. First-principles homogenization theory for periodic metamaterials. Phys Rev B 2011;84(7):075153.
[24] Craster RV, Kaplunov J, Pichugin AV. High-frequency homogenization for periodic media. P Roy Soc A 2010;466(2120):2341–62.
[25] Craster RV, Kaplunov J, Postnova J. High-frequency asymptotics, homogenisation and localisation for lattices. Quat J Mech Appl Math 2010;63(4):497–519.
[26] Nolde E, Craster RV, Kaplunov J. High frequency homogenization for structural mechanics. J Mech Phys Solids 2011;59(3):651–71.
[27] Antonakakis T, Craster RV, Guenneau S. Homogenisation for elastic photonic crystals and dynamic anisotropy. J Mech Phys Solids 2014;71:84–96.
[28] Nassar H, He QC, Auffray N. On asymptotic elastodynamic homogenization approaches for periodic media. J Mech Phys Solids 2016;88:274–90.
[29] Sridhar A, Kouznetsova VG, Geers MGD. Homogenization of locally resonant acoustic metamaterials towards an emergent enriched continuum. Comput Mech 2016;57(3):423–35.
[30] Sridhar A, Kouznetsova VG, Geers MGD. A semi-analytical approach towards plane wave analysis of local resonance metamaterials using a multiscale enriched continuum description. Int J Mech Sci 2017;133:188–98.
[31] Sridhar A, Kouznetsova VG, Geers MGD. A general multiscale framework for the emergent effective elastodynamics of metamaterials. J Mech Phys Solids 2018;111: 414–33.
[32] Koo S, Cho C, Jeong JH, Park N. Acoustic omni meta-atom for decoupled access to all octants of a wave parameter space. Nat commun 2016;7:13012.
[33] Muhlestein MB, Sieck CF, Wilson PS, Haberman MR. Experimental evidence of Willis coupling in a one-dimensional effective material element. Nat Commun 2017;8:15625.
[34] Quan L, Ra'di Y, Sounas DL, Alu A. Maximum Willis coupling in acoustic scatterers. Phys Rev Lett 2018;120(25):254301.

[35] Melnikov A, Chiang YK, Quan L, Oberst S, Alù A, Marburg S, Powell D. Acoustic meta-atom with experimentally verified maximum Willis coupling. Nat Commun 2019;10(1):3148.
[36] Groby JP, Malléjac M, Merkel A, Romero-García V, Tournat V, Torrent D, Li J. Analytical modeling of one-dimensional resonant asymmetric and reciprocal acoustic structures as Willis materials. New J Phys 2021;23(5):053020.
[37] Cho C, Wen X, Park N, Li J. Acoustic Willis meta-atom beyond the bounds of passivity and reciprocity. Commun Phys 2021;4(1):1–8.
[38] Zhai Y, Kwon HS, Popa BI. Active Willis metamaterials for ultracompact nonreciprocal linear acoustic devices. Phys Rev B 2019;99(22):220301.
[39] Ma F, Huang M, Xu Y, Wu JH. Bi-layer plate-type acoustic metamaterials with Willis coupling. J Appl Phys 2018;123(3):035104.
[40] Liu Y, Liang Z, Zhu J, Xia L, Mondain-Monval O, Brunet T, Alù A, Li J. Willis metamaterial on a structured beam. Phys Rev X 2019;9(1):011040.
[41] Meng Y, Hao Y, Guenneau S, Wang S, Li J. Willis coupling in water waves. New J Phys 2021;23(7):073004.
[42] Merkel A, Romero-García V, Groby JP, Li J, Christensen J. Unidirectional zero sonic reflection in passive PT-symmetric Willis media. Phys Rev B 2018;98(20):201102.
[43] Esfahlani H, Mazor Y. Alù A. Homogenization and design of acoustic Willis metasurfaces. Phys Rev B 2021;103(5):054306.
[44] Wiest T, Seepersad CC, Haberman MR. Robust design of an asymmetrically absorbing Willis acoustic metasurface subject to manufacturing-induced dimensional variations. J Acoust Soc Am 2022;151(1):216–31.
[45] Popa BI, Zhai Y, Kwon HS. Broadband sound barriers with bianisotropic metasurfaces. Nat Commun 2018;9(1):5299.
[46] Zhai Y, Kwon HS, Popa BI. Active Willis metamaterials for ultracompact nonreciprocal linear acoustic devices. Phys Rev B 2019;99(22):220301.
[47] Li ZN, Wang YZ, Wang YS. Tunable nonreciprocal transmission in nonlinear elastic wave metamaterial by initial stresses. Int J Solids Struct 2020;182:218–35.
[48] Li ZN, Wang YZ, Wang YS. Tunable mechanical diode of nonlinear elastic metamaterials induced by imperfect interface. P Roy Soc A 2021;477(2245):20200357.
[49] Wei LS, Wang YZ, Wang YS. Nonreciprocal transmission of nonlinear elastic wave metamaterials by incremental harmonic balance method. Int J Mech Sci 2020;173:105433.
[50] Lu Q, Wang YZ. Nonlinear solitary waves in particle metamaterials with local resonators. J Acoust Soc Am 2022;151(3):1449–63.
[51] Díaz-Rubio A, Tretyakov SA. Acoustic metasurfaces for scattering-free anomalous reflection and refraction. Phys Rev B 2017;96(12):125409.
[52] Li J, Shen C, Diaz-Rubio A, Tretyakov SA, Cummer SA. Systematic design and experimental demonstration of bianisotropic metasurfaces for scattering-free manipulation of acoustic wavefronts. Nat Commun 2018;9(1):1342.
[53] Chen Y, Li X, Hu G, Haberman MR, Huang G. An active mechanical Willis meta-layer with asymmetric polarizabilities. Nat Commun 2020;11(1):1–8.
[54] Craig SR, Su X, Norris A, Shi C. Experimental realization of acoustic bianisotropic gratings. Phys Rev Appl 2019;11(6):061002.
[55] Quan L, Yves S, Peng Y, Esfahlani H, Alù A. Odd Willis coupling induced by broken time-reversal symmetry. Nat Commun 2021;12(1):1–9.
[56] Muhlestein MB, Goldsberry BM, Norris AN, Haberman MR. Acoustic scattering from a fluid cylinder with Willis constitutive properties. P Roy Soc A 2018;474(2220):20180571.
[57] Lawrence AJ, Goldsberry BM, Wallen SP, Haberman MR. Numerical study of acoustic focusing using a bianisotropic acoustic lens. J Acoust Soc Am 2020;148(4):EL365.
[58] Qu HF, Liu XN, Hu GK. Topological valley states in sonic crystals with Willis coupling. Appl Phys Lett 2021;119(5):051903.
[59] Sepehrirahnama S, Oberst S, Chiang YK, Powell D. Acoustic radiation force and radiation torque beyond particles: effects of nonspherical shape and Willis coupling. Phys Rev E 2021;104(6–2):065003.
[60] Milton GW. New metamaterials with macroscopic behavior outside that of continuum elastodynamics. New J Phys 2007;9(10):359.
[61] Kweun JM, Lee HJ, Oh JH, Seung HM, Kim YY. Transmodal Fabry-Pérot resonance: theory and realization with elastic metamaterials. Phys Rev Lett 2017;118(20):205901.
[62] Yang X, Kweun JM, Kim YY. Theory for Perfect Transmodal Fabry-Perot interferometer. Sci Rep 2018;8(1):69.